SCIENTIFIC REPORTS

Strong enhancement of photoresponsivity with shrinking the electrodes spacing in few layer GaSe photodetectors

Yufei Cao[1]*, Kaiming Cai[1]*, Pingan Hu[2], Lixia Zhao[3], Tengfei Yan[1], Wengang Luo[1], Xinhui Zhang[1], Xiaoguang Wu[1], Kaiyou Wang[1] & Houzhi Zheng[1]

[1]SKLSM, Institute of Semiconductors, Chinese Academy of Science, P. O. Box 912, Beijing 100083, P. R. China, [2]KLMM, Harbin Institute of Technology, No. 2 YiKuang Street, Harbin, 150080, P.R. China, [3]Semiconductor Lighting Technology Research and Development Center, Institute of Semiconductors, Chinese Academy of Sciences, Beijing, 100083, P. R. China.

A critical challenge for the integration of optoelectronics is that photodetectors have relatively poor sensitivities at the nanometer scale. Generally, a large electrodes spacing in photodetectors is required to absorb sufficient light to maintain high photoresponsivity and reduce the dark current. However, this will limit the optoelectronic integration density. Through spatially resolved photocurrent investigation, we find that the photocurrent in metal-semiconductor-metal (MSM) photodetectors based on layered GaSe is mainly generated from the region close to the metal-GaSe interface with higher electrical potential. The photoresponsivity monotonically increases with shrinking the spacing distance before the direct tunneling happens, which was significantly enhanced up to 5,000 AW^{-1} for the bottom Ti/Au contacted device. It is more than 1,700-fold improvement over the previously reported results. The response time of the Ti/Au contacted devices is about 10–20 ms and reduced down to 270 μs for the devices with single layer graphene as metallic electrodes. A theoretical model has been developed to well explain the photoresponsivity for these two types of device configurations. Our findings realize reducing the size and improving the performance of 2D semiconductor based MSM photodetectors simultaneously, which could pave the way for future high density integration of optoelectronics with high performances.

The planar metal-semiconductor-metal (MSM) photodetectors based on layered materials have been studied extensively in recent years[1–5]. This is because the planar MSM photodetector has many advantages, such as compatibility with current semiconducting technology, very low dark current and high operation speed, which are attractive for many optoelectronic applications[6–8]. However, only relative small photoresponsivity was observed in these two dimensional (2D) layered materials based MSM photodetectors including graphene (less than 0.1 AW^{-1}) and MoS$_2$ (no more than 7.5 mAW^{-1})[4,9–11], which is because of the weak optical absorption or very small carrier mobility in these layered materials. In order to improve the photoresponsivity, graphene based photodetector has focused on enhancement of the absorption of light in graphene, for example by exploiting thermoelectric effects[12,13], microcavities[14,15] or multilayer tunneling structure[16] to improve its photoresponsivity up to 1,000 AW^{-1}. By improving the device mobility, the MoS$_2$ based photodetectors have reached a maximum external photoresponsivity of 880 AW^{-1} (ref. 17). However, so far relative large device sizes were used in those investigations, impeding the high integration density applications. Since the importance of the device size and the photoresponsivity, we systematically investigated the relation between the photoresponsivity and the electrodes spacing for both the top and bottom contacted MSM photodetectors based on layered GaSe. Combining the photocurrent measurements under global and spatially resolved illuminations[18], a model has been developed for understanding the underlying physics of photoresponsivity in our MSM photodetectors. Our work suggests that MSM photodetectors based on high photoresponse layered materials can be used for future high density optoelectronic applications.

The layered hexagonal GaSe was chosen to be the optical active material in this work because of its high photoresponsivity (2.8 AW^{-1}) and quantum efficiency (1,367%), which was demonstrated recently[19]. The GaSe crystals are composed of vertically stacked Se-Ga-Ga-Se sheets weakly bound by van der Waals interactions.

Usually it is a p-type semiconductor (Supplementary Fig. S1) with an indirect bandgap of ~2.11 eV at the center of the Brilliouin zone, which is only 25 meV above the conduction band minimum[19,20]. Since the very small energy difference between the indirect and direct bandgap, the photoexcited carriers can be easily transferred between these two bands with thermal fluctuation. Therefore, GaSe can serve as a promising material for optoelectronic applications. Furthermore, the optoelectronic devices based on layered GaSe can not only be used as visible and ultraviolet photodetectors[19,21], THz source generator[22], but also for the nonlinear optical applications due to its large nonlinear optical coefficient (54 pmV^{-1})[23].

Results

Sample preparation and characterization. Since the metal-semiconductor contacting regime could play a very important role in the MSM photodetectors[24–26], the devices with two different types of designs were fabricated based on mechanical exfoliated few layer GaSe nanosheet[27]. For the top contacted devices, a few layer of GaSe was exfoliated first on the Si/SiO$_2$ substrate, and then the metal contacts were deposited on top of it. While for the bottom contacted devices, the metal contacts were deposited first on Si/SiO$_2$ and then the GaSe was exfoliated on the metal contacts. It should be noted that the interface of the contacts between these two types of devices is slightly different, where the bottom contacted device is Ti/Au/GaSe interface while the top contacted one is GaSe/Ti (2 nm)/Au. The schematic illustrations of our devices are presented in Fig. 1a,b (see device fabrication Method). In order to improve the response time of the photodetectors, the devices with top single layer graphene electrodes have also been fabricated (see device fabrication Method). The thickness of the GaSe flakes was determined by atomic force microscopy (AFM) (see Supplementary Fig. S2 for more details). The typical thickness used for the sensitive photodetectors in this work is about ~20–30 nm. The normalized photocurrent spectrum of the photodetectors with wavelength range from 390 to 800 nm shows two well-defined peaks (Fig. 1c), where one peak is located at 412 nm corresponding to an energy gap of 3.01 eV and the other one is located at 610 nm corresponding to 2.03 eV. These two energy gaps correspond to the transition from p_x and p_y-like orbits to the conduction band and p_z-like orbit to the conduction band, respectively[21]. The band gap generally increases as the thickness of layers approaches atomic dimensions for the layered materials. The

monolayer has a degenerated direct and indirect band gap at 2.1 eV (590 nm) and the bulk form GaSe has a band gap at around 2.0 eV (619 nm)[19,21]. To achieve an ideal photoresponse, the wavelength at 410 nm was chosen for the following studies presented in this work.

Photoresponsivity with global illumination. To investigate the spacing distance and the device configuration effect on the enhancement of the photoresponsivity, photocurrent measurements were carried out for both type devices with different spacing distances between the source and drain electrodes. Fig. 2a shows the SEM image of a device with top contacted devices and distance between each electrode from bottom to up are 0.09, 0.2, 0.5, 1, 5 and 10 μm, respectively. Current-voltage curves of devices were recorded with sweeping bias voltage under global illumination (λ = 410 nm) with light intensity ranging from 1×10^{-2} to 1.45 mWcm^{-2}. The photocurrent is the difference between the current under illumination and the dark current, namely $I_{ph} = I_{light} - I_{dark}$. In order to directly compare the photoresponsivity for both the bottom and top contacted devices, only the device area between the source and drain electrodes was counted for the calculation of the photoresponsivity, which is described as $R = I_{ph}/P_{light}$ with $P_{light} = WlL_{intensity}$ for the very thin nanosheet, where $L_{intensity}$ is the light intensity, W is the width of the device, and l is the distance between the source and drain electrodes. With the bias voltage above 2 V, the photoresponsivity is rigidly associated with the lateral spacing distance for both the bottom and top contacted devices with fixed contact width (Fig. 2b; Supplementary Fig. S3b). With reducing the distance between the electrodes, the photoresponsivity rapidly increases at fixed V_{DS} = 8 V and light intensity 0.01 mWcm^{-2}. Very low dark current was observed for both the top and bottom contacted devices with $l >$ 200 nm. This is because the dark current is mainly determined by the two back to back Schottky barriers of the devices. However, the distance l can't be cut too short since the direct tunneling will happen between the source and drain under applied bias at very small l, which will enlarge the dark current and reduce the sensitivity of the photodetector. To ensure the low dark current, we found that the dark current starts to increase with the applied voltages above 10 V for the device with l = 200 nm (Fig. 2c). Furthermore, very large dark current was observed with V_{DS} above 0.2 V for the device with l = 90 nm (Fig. 2c, inset). Moreover, the photoresponsivity of the bottom contacted devices increases from 200 to 5,000 AW^{-1} with l shrinking
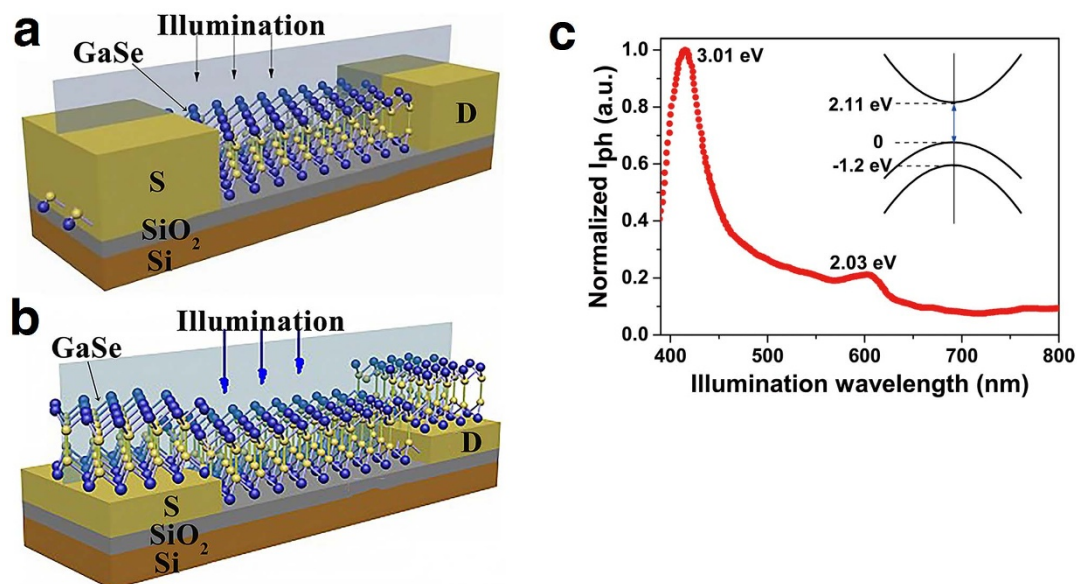

Figure 1 | Photodetector structure. (a) A schematic of the photodetector with the contacts at the top. (b) A schematic of the photodetector with the contacts at the bottom. (c) The normalized photocurrent of the GaSe photodetector as a function of the illumination wavelength.
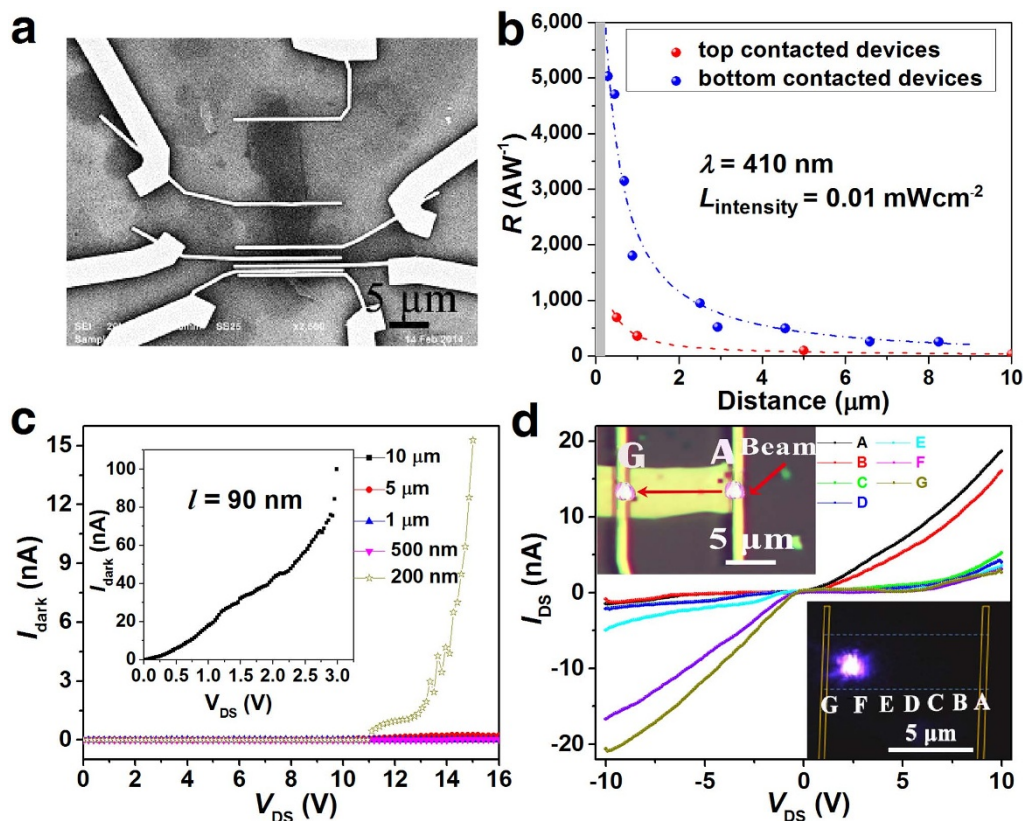
Figure 2 | Both top and bottom contacted photodetectors with different spacing distance. (a) The scanning electron microscopy image of the typical top contacted MSM photodetectors with Scale bar of 5 μm. The smallest spacing distances between the metal fingers is 90 nm and the finger width is 700 nm. (b) The photoresponsivity as a function of the spacing distances at $V_{DS} = 8$ V for both the top contacted (red) and bottom contacted (blue) photodetectors, where the dash lines are the fitting results using our models. The direct tunneling is appeared under bias in the grey area with $l \leq 200$ nm, which will decrease the photoresponsivity. (c) Dark current voltage characteristics for the photodetectors with different spacing distances. (d) Current voltage characteristic of spatially resolved localized illumination. The up left inset shows the device image and the position of illumination. Bottom right inset shows the spots of the illumination.

from 8 μm to 290 nm, while it only increases from 40 to 900 AW^{-1} for the top contacted devices. Thus we can conclude that the highest photoresponsivity can be achieved in the bottom contacted photo-detectors with optimized nanoscale spacing distance.

Photoresponsivity with localized illumination. For searching the nature of the photoresponsivity enhancement with shrinking the photodetector size, the localized laser beam with spot diameter of 1.5 μm was used to investigate the spatially resolved photocurrent in a rather wide top contacted device with $l = 9$ μm (Fig. 2b,d, inset). Seven points were marked out as Point A ~ G with spacing about 1.5 μm between the adjacent points (Fig. 2d, inset). Independent of the bias direction, very small currents during sweeping the voltages were observed when the localized irradiating laser was located in the middle of the device, namely the marked Points C, D, and E. However, when the laser was focused on the positions A and B, the photocurrents increased obviously up to ten times of the current that from C ~ E positions under a forward bias voltage, i.e., a positive voltage is applied to the electrode near the A and B spots. Similarly, the magnitude of the photocurrents under a negative bias voltage with illumination at positions F and G were as high as those for Point A and B (Fig. 2d, inset). Measurements of photocurrents with light irradiation at different localized positions clearly demonstrate that the photocurrent is mainly generated from the photoexcited carriers close to the metal semi-conductor contacts. Furthermore, the photocurrent active region is always close to the Schottky barrier with higher electrical potential.

The underlying physics of the current-voltage results with spatially localized laser illumination can be understood according to the band

diagram analysis. With no illumination and drain bias voltage, the device is in its equilibrium state, characterized by Schottky barriers at the contacts. Considering GaSe as a p-type material with Fermi energy of around 5.6 eV, which is larger than the Au work function[28], we plotted the schematic band diagram of the devices (Fig. 3a,b). Illuminating the device under zero bias, with photons energy higher than bandgap, electron-hole pairs will be generated and separated in the depletion region of GaSe. However, both the photoexcited electrons and holes moved to the opposite directions at the two end Schottky barriers, which will compensate each other, as indicated in Fig. 3a. While the electron-hole pairs outside the depletion region of Schottky barrier will diffuse randomly due to the absence of electric field. As a result, the photocurrent was hardly detected under global illumination with zero bias.

Under spatially resolved illumination, the mechanism of the asymmetric photocurrent results can be divided into three situations where the localized laser was focused on the left, middle and right part of the GaSe nanosheet (taking situation with forward bias voltage as an example). For irradiation on the middle points, which is located outside of the Schottky barrier, the photogenerated electrons and holes are separated by the electric field. The electrons are drifted to the right while the holes are drifted to the left. Carriers need to travel to the metal contacts before being collected, which will mostly be recombined due to the relative small mobility (Supplementary Fig. S1) and result in a weak photocurrent. With illuminating on the right side, the built-in electric field and the electric field built by bias voltage have the same direction in the right Schottky depletion region, which will separate the photogenerated carriers more effi-
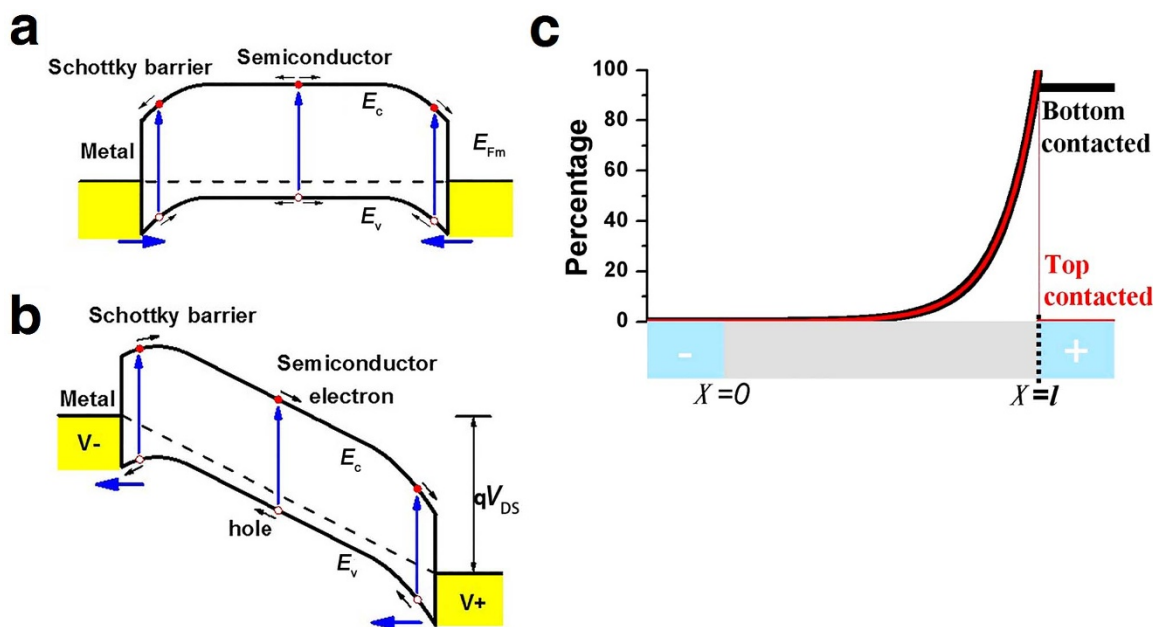
Figure 3 | Schematic band diagrams and the possibility of the photoexcited electrons can reach to the interface at high electrical potential side of the MSM devices. (a) Band diagram of the photodetector with zero bias voltage under global illumination. (b) Band diagram of the photodetector with forward bias voltage under global illumination. (c) The schematic diagram of the possibility of the photoexcited electrons at forward bias can reach to the interface at high electrical potential side for both the top contacted (red line) and bottom contacted devices (black line).

ciently. Since holes need to drift from right side to left side, most of the photoexcited holes are scattered or recombined. Thus the photocurrent is mainly originated from the photoexcited electrons tunneling though the barriers. While with illuminating on the left side at forward bias, the built-in field in Schottky depletion region and the electric field built by the bias voltage were just in the opposite direction, which will cancel each other, thus the photogenerated carriers were separated more difficultly and tiny photocurrent was observed. Conversely the spatially resolved photocurrent shows opposite phenomenon under reverse bias, which is because of the opposite electrical potential direction and thus the band diagram.

The asymmetric photocurrent is found to be more sensitive to the photoexcited carriers close to the Schottky barrier at the higher electrical potential end, which should also be valid under global illumination. The Schottky barrier width determines the effective absorption area, while the barrier width and height together define the carrier tunneling probability. In addition, the built-in electric field within the barrier and the external electric field determine the speed of separated carriers together. The width of the Schottky barrier gets thinner under the bias voltage when the built-in electric field has the same direction to the electric field direction built by the bias voltage. These can explain why the current increases with increasing the bias voltage in the meantime at fixed light intensity.

Discussion

We developed a theoretical model to demonstrate the concept related to the transport of photogenerated carriers in a metal-semiconductor-metal (MSM) photodetector. By solving the continuity equations for carriers in the region of the device based on the measured device structure (see Supplementary Fig. S4 and S5 for more details), this model accurately depicts the dependence of the photoresponsivity on spacing distance, as shown in Fig. 2b. For clarity and simplicity, at forward bias, the electrons were considered as the main carrier to generate the photocurrent. The photogenerated electrons diffuse to the interface between the GaSe and the metal contact with higher electrical potential (using $X = l$ at forward bias for example), and then the electrons have the same possibility to pass through the

interface and enter into the metal contact. This model is not suitable for the extreme small devices with existing the direct tunneling between the source and drain. Luckily, the direct tunneling should be avoided in photodetectors.

For the top contacted device, the possibility of the photogenerated electrons at any arbitrary position $X = x$ in the channel reaching to the interface $X = l$ can be written down as: $\exp[-(l-x)/v\tau]$ (red line of Fig. 3c), where v is the electron velocity and τ is the lifetime of the electrons. Then the total number of photogenerated electrons reached to $X = l$ per second under global illumination is

$$N = \int_0^l (\sigma W)\exp[-(l-x)/L_D]\mathrm{d}x = \sigma W L_D[1 - \exp(-l/L_D)] \qquad (1)$$

where σ is the number of the photogenerated electrons per square meter, and $L_D = v\tau$ is the diffusion length. And the photocurrent is proportional to the number of total carriers per second received at $X = l$, namely $I_{ph} = cN = c\sigma W L_D[1 - \exp(-l/L_D)]$, where c is a constant as the coefficient of proportionality. Under this model, the photoresponsivity thus can be written down as $R = I_{ph}/P_{light} = C_0[1 - \exp(-l/L_D)]/l$, where $C_0 = c\sigma L_D/L_{intensity}$. Using this model, the spacing distance between the source drain electrodes dependence of the photoresponsivity for the top contacted devices can be well fitted using the photoresponsivity equation, where the diffusion length of the electrons $L_D = 170$ nm was obtained.

However, for the bottom contacted devices, except for the photocurrent contribution described above, the photoexcited electrons in the both contacted regions also contribute to the photocurrent under global illumination. The photogenerated electrons in the left contact region have to diffuse to the right side and then enter into the metal contacts at forward bias, which can be described similarly using the above formula. However, the photoexcited electrons in right contact side will have vertical rather than planar transport and then enter into the metal contact below, which have large contribution to the photocurrent (black line of Fig. 3c). Thus the photocurrent for the bottom contacted device is the sum of the planar and vertical contribution, which can be written down as:
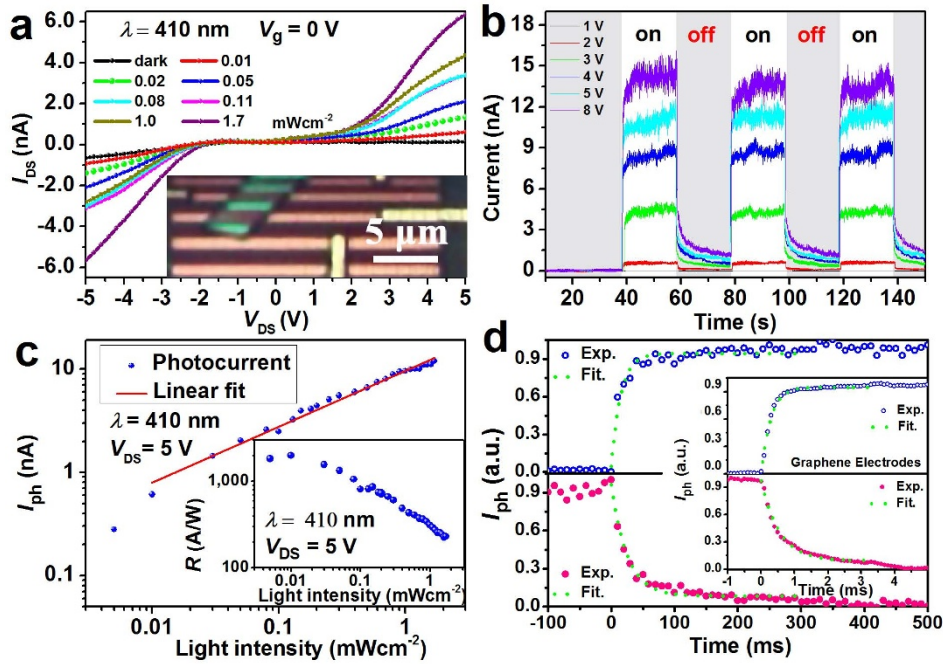
Figure 4 | Bottom contacted photodetector with 1 μm spacing distance. (a) Photocurrent as a function of the drain voltage under global illumination with different light intensities at fixed wavelength of 410 nm. Inset shows the optical image of the device. (b) Time-resolved photoresponse of the photodetector, recorded for different bias voltages V_{DS} with fixed light intensity $P_{light} = 1.7$ mWcm^{-2}. The period of the laser on and off is 20 seconds. (c) Photocurrent as a function of the light intensity at fixed bias voltage $V_{DS} = 5$ V, where the red line is the fitting result. Inset shows the light intensity dependence of the photoresponsivity at fixed bias voltage $V_{DS} = 5$ V. (d) The rise and decay of the normalized photocurrent at the initial stage just after the laser is switched on (upper panel) and off (lower panel), where the dots are the experimental results and the dash dots are the fitting results. Inset shows the rise (upper panel) and decay (lower panel) of the normalize photocurrent for the photodetectors with single layer graphene as electrodes.

$$I_{ph} = c \int_{-L_1}^{l} (\sigma W) \exp[-(l-x)/L_D]dx +$$
$$c' \int_{0}^{d} (\sigma W L_r) \exp[-(d-x)/L'_D]dx \qquad (2)$$

where L_1 is the width of left contact, c' is the probability of vertical transport electrons entering into the metal contact, L_r is the width of the right contact, and L'_D is the vertical diffusion length. Thus the photoresponsivity then can be written down as:

$$R = I_{ph}/P_{light} = C_0\{1 - \exp[-(l+L_1)/L_D]\}/l +$$
$$C_1[1 - \exp(-d/L'_D)]/l \qquad (3)$$

where the coefficient $C_1 = c'\sigma L_r L'_D / dL_{intensity}$. Normalized the experimental contacts width, the distance dependence of the photoresponsivity for the bottom contacted devices can be well described (Fig. 2b).

Taking the advantage of the bottom contacted device, we then pick out one of the typical bottom contacted photodetector with spacing $l = 1$ μm between the two electrodes as example to carefully investigate the bias voltages, time, and photointensity dependence of the photocurrent. The optical image of the device is shown in the inset of Fig. 4a. The current as a function of the bias voltage under dark and global illumination at different irradiation intensities was shown in Fig. 4a. Very low dark current was observed in measured voltage regime, which is benefit from the device structure with two back to back Schottky barriers. Under global illumination, the current starts to increase with the applied voltages at ±2 V, which increases further with increasing the magnitude of the voltages. Also the current increases with increasing the light intensities. Current was signifi-

cantly increased by two orders of magnitude, from 40 pA (dark condition) to ~6 nA at fixed light intensity ~1.7 mWcm^{-2} and bias voltage 5 V. This increase is much larger than that of top contacted device, where it only increased from 40 pA to 1.76 nA at the same bias and light intensity. The large difference of the photocurrent is due to the contribution of the photoexcited carriers from the bottom contacted device. We then probed the time-dependent photoresponse to the global illumination with light intensity 1.7 mWcm^{-2} at different bias voltages (Fig. 4b). With $V_{DS} = 1$ V, nothing was clearly observed with switching light on and off. With V_{DS} above 2 V, the current sharply increases with switching on the light and drops dramatically after the light switched off, which is consistent with the current-voltage results under illumination (Fig. 4a).

Based on measurements of Fig. 4a,b, the light intensity dependence of the photocurrent was plotted in Fig. 4c. It can be fitted to a power law $I_{ph} \propto P^\gamma$, where $\gamma = 0.54$ determines the response of the photocurrent to the light intensity[31,32]. The non-unity exponent suggests a complex process of electron-hole generation, recombination and trapping within the semiconductor[31,33]. With decreasing the light intensity at fixed bias voltage $V_{DS} = 5$ V, the corresponding photoresponsivity firstly increases and reaches the maximum of 1,200 AW^{-1} (Fig. 4c, inset), which is more than 400 times higher than the previously reported GaSe photodetector[19] and five orders higher than that of graphene-based photodetectors[4,34,35]. Then the photoresponsivity decreases with increasing the photointensity for the light intensity above 0.01 mWcm^{-2} (Fig. 4c, inset). This is because that the light absorption efficiency reaches to the maximum in this few-layer photodetector at relatively low photointensity of 0.01 mWcm^{-2}. The light intensity dependence of the photocurrent and photoresponsivity at different bias voltages was also investigated (Supplementary Fig. S3).

The sensitive, fast and reversible switching between the on and off states allows the device to act as high quality photo detectors and switchers. The dynamic response to the light illumination for rise and

fall in our devices can be expressed by $I(t) = I_0[1-\exp(-t/\tau_r)]$ and $I(t) = I_0\exp(-t/\tau_d)$, where τ_r and τ_d are the time constants for the rise and decay (Fig. 4d). The rising and falling time can be obtained by fitting the experimental results, which is shown in Fig. 4d. The photocurrent rose dramatically in 10 ms after the light illumination and decayed within 20 ms after the light-off. This is in sharp contrast to the long tails up to a few seconds after the sharp rising and falling in the previous reported few layer GaSe photodetectors, a much shorter rising and falling tails about 0.2 s with light shining on and off were observed, which is originated from cutting away the photo-generated electrons far away from the interface at the high potential side. The evaluated rising and falling speed of our photodetectors is one of the fastest among the reported data for layered material-based photodetectors[11,29]. However, this speed is still much slower than that usually observed MSM photodetectors[30], which can be attributed to the influences of trap states in GaSe or the interfaces. The rising and falling time can be improved using other materials to optimize the Schottky barrier and have better interface quality. With single layer graphene as metallic electrodes, the rising and falling time can be significantly reduced down to ~270 μs and ~550 μs, respectively, which is about two orders magnitude faster than that of the devices with the Ti/Au electrodes (inset of Fig. 4d).

In summary, significant improvements in photosensitivity can be realized with shrinking the spacing distance in the layered GaSe based MSM photodetectors[19], which is more than 3 orders improvement with shrinking l down to 290 nm for the bottom contacted MSM photodetectors. Although the rising and falling time is about 10 and 20 ms and not very sensitive to the device size for the Ti/Au contacted devices, the response time of the device can be further reduced down to 270 μs using single layer graphene as electrodes, which is about two orders magnitude faster than that of the devices with Ti/Au electrodes. From a broad perspective, we have developed a model for understanding the underlying physics of the photo-current in our MSM photodetectors, which could also be widely used in any low dimensional materials based MSM photodetectors. Our work suggests that it is feasible to design bottom contacted nanoscale MSM photodetectors based on layered materials with high photo-responsivity, which will open pathways for future integrated optoelectronic applications.

Methods

Device fabrication. The GaSe single crystal and the single layer graphene used in this work were grown using a chemical vapour deposition (CVD) process. The GaSe flakes were prepared by mechanical exfoliation of the GaSe single crystal. GaSe flakes were identified by optical microscope and their thicknesses were further confirmed by AFM. Devices with two types of contacts were fabricated: bottom contacted electrodes and top contacted electrodes. We firstly pre-patterned the alignment marks using optical lithography on a SiO_2(300 nm)/Si^{++} substrate. For the top contacted devices, firstly the few layer of GaSe was exfoliated on the Si/SiO_2 substrate, and then the metal contacts Ti/Au (2/80 nm) were deposited using thermal evaporator. While for the bottom contacted devices, the metal contacts Ti/Au (2/40 nm) with designed width 700 nm were thermally evaporated first and then the GaSe was exfoliated on it. For the devices with single layer graphene electrodes, after the transfer of the GaSe flakes onto the substrate, the patterned graphene strips were transferred onto the GaSe flakes as electrodes with 2–3 μm width of overlaps on the edges of GaSe flakes. The distance between two graphene electrodes is about 5 μm. The metal electrodes for wire bonding were patterned on the non-overlapping region of graphene by electron-beam lithography (EBL) and deposition of Ti/Au (3/100 nm) thin film by thermal evaporator. SEM images in the manuscript were performed using a JEOL JSM6510 operated at 20 KV with LaP_6 filament.

Electrical measurements. All electrical and optoelectrical measurements were measured using Agilent Technology B1500A under vacuum of 10^{-6} mbar at room temperature. The as-prepared samples behaved in a p-type manner from FET results. GaSe nanosheet sample have a very low mobility as 5×10^{-3} cm^2 $V^{-1}s^{-1}$.

Global illumination measurements. Monochromatic illumination was provided by a Zolix Omni-λ300 monochrometer with a Fianium WhiteLase Supercontinuum Laser Source with repetition rate 20 MHz. The output laser wavelength can be tuned by monochromator Omni-λ 300. The laser beams could directly irradiate the nanosheet device through a transparent glass window of the vacuum chamber. The laser spot size is about 1 mm² on the sample for the optoelectrical measurements under global illumination.

Spatially resolved photocurrent measurements. A microscope objective and a micromechanical stage were used to localize the corresponding position of the focused laser beam on the photodetector, where the diameter of the laser spot size was about 1.5 μm and the illumination power was fixed at 1 μW. The current-voltage (I–V) measurements were performed with the spatially resolved localized laser from A to G positions.

1. Liu, F. C. *et al.* High-Sensitivity Photodetectors Based on Multilayer GaTe Flakes. *ACS Nano* **8**, 752–760 (2014).
2. Zhang, W. J. *et al.* Ultrahigh-Gain Photodetectors Based on Atomically Thin Graphene-MoS$_2$ Heterostructures. *Sci. Rep.* **4**, 3826 (2014).
3. Li, H. M. *et al.* Metal-semiconductor barrier modulation for high photoresponse in transition metal dichalcogenide field effect transistors. *Sci. Rep.* **4**, 4041 (2014).
4. Mueller, T., Xia, F. N. A. & Avouris, P. Graphene photodetectors for high-speed optical communications. *Nat. Photonics* **4**, 297–301 (2010).
5. Konstantatos, G. *et al.* Hybrid graphene-quantum dot phototransistors with ultrahigh gain. *Nat. Nanotechnol.* **7**, 363–368 (2012).
6. Fang, X. *et al.* An Efficient Way to Assemble ZnS Nanobelts as Ultraviolet-Light Sensors with Enhanced Photocurrent and Stability. *Adv. Funct. Mater.* **20**, 500–508 (2010).
7. Fang, X. *et al.* New Ultraviolet Photodetector Based on Individual Nb$_2$O$_5$ Nanobelts. *Adv. Funct. Mater.* **21**, 3907–3915 (2011).
8. Guo, F. W. *et al.* A nanocomposite ultraviolet photodetector based on interfacial trap-controlled charge injection. *Nat. Nanotechnol.* **7**, 798–802 (2012).
9. Tsai, D. S. *et al.* Few-Layer MoS2 with High Broadband Photogain and Fast Optical Switching for Use in Harsh Environments. *ACS Nano* **7**, 3905–3911 (2013).
10. Gan, X. T. *et al.* Chip-integrated ultrafast graphene photodetector with high responsivity. *Nat. Photonics* **7**, 883–887 (2013).
11. Yin, Z. Y. *et al.* Single-Layer MoS$_2$ Phototransistors. *ACS Nano* **6**, 74–80 (2012).
12. Lemme, M. *et al.* Gate-activated photoresponse in a graphene p–n junction. *Nano Lett.* **11**, 4134–4137 (2011).
13. Gabor, N. M. *et al.* Hot carrier–assisted intrinsic photoresponse in graphene. *Science* **334**, 648–652 (2011).
14. Furchi, M. *et al.* Microcavity-Integrated Graphene Photodetector. *Nano Lett.* **12**, 2773–2777 (2012).
15. Engel, M. *et al.* Light-matter interaction in a microcavity-controlled graphene transistor. *Nat. Commun.* **3**, 906 (2012).
16. Liu, C. H., Chang, Y. C., Norris, T. B. & Zhong, Z. Graphene photodetectors with ultra-broadband and high responsivity at room temperature. *Nat. Nanotechnol.* **9**, 273–278 (2014).
17. Lopez-Sanchez, O., Lembke, D., Kayci, M., Radenovic, A. & Kis, A. Ultrasensitive photodetectors based on monolayer MoS$_2$. *Nat. Nanotechnol.* **8**, 497–501 (2013).
18. Liu, Y., Yang, Q., Zhang, Y., Yang, Z. Y. & Wang, Z. L. Nanowire Piezo-phototronic Photodetector: Theory and Experimental Design. *Adv. Mater.* **24**, 1410–1417 (2012).
19. Hu, P. A., Wen, Z. Z., Wang, L. F., Tan, P. H. & Xiao, K. Synthesis of Few-Layer GaSe Nanosheets for High Performance Photodetectors. *ACS Nano* **6**, 5988–5994 (2012).
20. Zhu, Z. Y., Cheng, Y. C. & Schwingenschlogl, U. Topological Phase Transition in Layered GaS and GaSe. *Phys. Rev. Lett.* **108**, 266805 (2012).
21. Lei, S. D. *et al.* Synthesis and Photoresponse of Large GaSe Atomic Layers. *Nano Lett.* **13**, 2777–2781 (2013).
22. Schubert, O. *et al.* Sub-cycle control of terahertz high-harmonic generation by dynamical Bloch oscillations. *Nat. Photonics* **8**, 119–123 (2014).
23. Kübler, C., Huber, R., Tübel, S. & Leitenstorfer, A. Ultrabroadband detection of multi-terahertz field transients with GaSe electro-optic sensors: Approaching the near infrared. *Appl. Phys. Lett.* **85**, 3360 (2004).
24. Wang, J. F., Gudiksen, M. S., Duan, X. F., Cui, Y. & Lieber, C. M. Highly polarized photoluminescence and photodetection from single indium phosphide nanowires. *Science* **293**, 1455–1457 (2001).
25. Lee, E. J. H., Balasubramanian, K., Weitz, R. T., Burghard, M. & Kern, K. Contact and edge effects in graphene devices. *Nat. Nanotechnol.* **3**, 486–490 (2008).
26. Sobhani, A. *et al.* Narrowband photodetection in the near-infrared with a plasmon-induced hot electron device. *Nat. Commun.* **4**, 1643 (2013).
27. Novoselov, K. S. *et al.* Electric field effect in atomically thin carbon films. *Science* **306**, 666–669 (2004).
28. Bose, D. N. & Pal, S. Schottky barriers on anisotropic semiconductor GaTe. *Philos. Mag. B* **75**, 311–318 (1997).
29. Chitara, B., Panchakarla, L. S., Krupanidhi, S. B. & Rao, C. N. R. Infrared Photodetectors Based on Reduced Graphene Oxide and Graphene Nanoribbons. *Adv. Mater.* **23**, 5419 (2011).
30. Tang, L. *et al.* Nanometre-scale germanium photodetector enhanced by a near-infrared dipole antenna. *Nat. Photonics* **2**, 226–229 (2008).
31. Rose, A. *Concepts in Photoconductivity and Allied Problems,* Krieger Publishing Company, New York 1978.
32. Yang, S. *et al.* High performance few-layer GaS photodetector and its unique photo-response in different gas environments. *Nanoscale* **6**, 2582–2587 (2014).

33. Kind, H., Yan, H. Q., Messer, B., Law, M. & Yang, P. D. Nanowire ultraviolet photodetectors and optical switches. *Adv. Mater.* **14**, 158 (2002).
34. Xia, F. N., Mueller, T., Lin, Y. M., Valdes-Garcia, A. & Avouris, P. Ultrafast graphene photodetector. *Nat. Nanotechnol.* **4**, 839–843 (2009).
35. Pospischil, A. *et al.* CMOS-compatible graphene photodetector covering all optical communication bands. *Nat. Photonics* **7**, 892–896 (2013).

Acknowledgments

Author contributions

K.W. conceived and designed the experiments. P.H. provided the high quality CVD growth GaSe single crystals. Y.C., K.C. and W.L. fabricated the devices. T.Y. helped for the spatially resolved measurements. Y.C. and K.C. performed the measurements. Y.C., K.C., L.Z., X.Z., X.W., H.Z. and K.W. analyzed the test results and revised the manuscript. All authors discussed and commented on the manuscript.

Additional information